Semnan University

Journal of Heat and Mass Transfer Research

Journal homepage: http://jhmtr.journals.semnan.ac.ir

Numerical Study of Entropy Generation for Natural Convection in Cylindrical Cavities

Abdollah Rezvani, Mohammad Sadegh Valipour, Mojtaba Biglari *

Faculty of Mechanical Engineering, Semnan University, Semnan, Iran

PAPER INFO

History:

Submitted 19 August 2014
Revised 18 december 2014
Accepted 30 march 2015

Keywords:

Artificial compressibility
Entropy
Explicit finite-volume method
Natural convection Nusselt number

A B S T R A C T

In this paper, an enhanced computational code was developed using a finite-volume method for solving the incompressible natural convection flow within cylindrical cavities. Grids were generated by an easy method with a view to providing a computer program. An explicit integration algorithm was applied to find the steady-state condition. Also, instead of the conventional algorithms of SIMPLE (Semi Implicit Method) and SIMPLEC (Semi-Implicit Method for Pressure Linked Equations–Consistent), an artificial compressibility technique was applied for coupling the continuity to the momentum equations. The entropy generation, which is a representation of the irreversibility and efficiency loss in engineering the heat-transfer processes, has been analyzed in detail. The discretization of the diffusion terms is simplified greatly using an enhanced scheme similar to the flux averaging in the convective terms. Additionally, an analysis of the entropy generation in a cylindrical enclosure is performed. In order to show the validation of this study, the code is reproduced to solve a similar problem from the cited paper. Finally, the solutions were extended for the new cases.

DOI: 10.22075/jhmtr.2015.347

1. Introduction

Natural convection in enclosures is a kind of classical problem in heat transfer and numerical heat transfer, and many experimental and theoretical studies have been performed, including those on thermal storage, environmental comfort, grain drying, furnaces, cooling of electronic devices, double-glazed windows, and solar collectors. Whatever the shape of the wall, flow and heat transfer inside enclosures have numerous engineering applications, such as heat exchangers, energy storage, solar collectors, double-wall insulation, electric machinery, cooling systems for electronic devices, and natural circulation in the atmosphere [1-11].

Natural convection flow into the cylindrical cavities could be used in energy-storage equipment such as the longitudinal cylindrical pipes installed in the back of the natural gas transmission pipeline terminals near cities filled by natural gases.

This storage method is useful, especially in the cold season when gas pressure falls. The integrated flat-plate solar collectors are the other examples related to the present study. In these collectors, the fluid as an absorber has flow into the longitudinal cylindrical pipe.

Heat-transfer processes and devices are inherently irreversible. Energy conservation requires the use of efficient thermodynamic heat-transfer processes, that is, minimization of irreversibility (entropy

Corresponding Author: *Mojtaba Biglari*, Faculty of mechanical engineering, Semnan University, Semnan, Iran
Email: Rezvani_61@semnan.ac.ir

generation) due to temperature gradients and viscous dissipation [12-16].

There are a fair amount of studies about natural convection heat-transport problems in the literature. The optimal design criteria for thermal systems that minimize their entropy generation recently have been a topic of great interest, especially in the fields related to the geometry of a duct and natural convection in the enclosure. The present paper reports a numerical study of entropy generation in the incompressible natural convection flow within cylindrical cavities. Attempts are made to analyze the influence of the Rayleigh number, aspect ratio, and irreversibility distribution ratio on entropy production. Therefore, it is essential that an engineer focus on the irreversibility of heat-transfer and fluid-flow processes and try to establish the optimal design criteria for thermodynamic systems.

In the last numerical solutions of the heat transfer and fluid flow for enclosures, a code based on the enhanced SIMPLE method [17] couples the pressure with the velocity. In the current work, an artificial compressibility technique was applied to couple the continuity with the momentum equations. The idea of relaxing the incompressibility constraint by adding an artificial compressibility term has been known for a long time and has been used extensively in finite-volume as well as in finite-element approximations of the incompressible Navier–Stokes equations [18-20].

In a finite-volume method, mapping is not needed. Therefore, the scheme is applied directly in the physical domain. Among the various schemes proposed for the flux calculation in the finite-volume model, the Jameson's numerical method is still of use because of its simplicity [21]. In this work, the Jameson's flux-averaging finite-volume scheme for space discretization was developed.

One of the methods for solving incompressible flows is based on the artificial compressibility formulation of Chorin [22]. The artificial compressibility approach circumvents the difficulty of the pressure decoupling in the incompressible Navier–Stokes equations by adding a pseudo-time pressure derivative to the continuity equation. Then, the new system of equations can be iterated in pseudo-time until the divergence-free flow field is satisfied. The method can be used both for steady and unsteady flows, and there are a number of papers in the literature that describe implicit and explicit strategies for solving steady and unsteady flow problems in conjunction with artificial compressibility [23-31].

The artificial compressibility method leads to hyperbolic and hyperbolic–parabolic equations for inviscid and viscous incompressible (constant density) flows, respectively. The discretization schemes and solvers developed for artificial compressibility have many similarities with the methods developed for compressible flows. Therefore, numerical developments for compressible flows can be transferred to incompressible flows. Although artificial compressibility has been used extensively for constant-density flows, the development of numerical schemes in the framework of artificial compressibility for variable-density incompressible flows have received scant attention in the literature. Riedel [32] used an artificial compressibility formulation to construct an unstructured finite volume method for the solution of two-dimensional steady viscous, incompressible, reacting flows, while Lin and Jion [33] developed a surface-capturing total variation diminishing method with slope modification for a multi-fluid incompressible Navier–Stokes formulation.

To suppress the tendency for odd and even point decoupling, the artificial dissipation terms are added in the central differencing schemes. In this work, in order to overcome this problem, the discretization of the viscous and thermal conduction terms were simplified greatly using an enhanced scheme similar to the flux averaging in the convective term so that the artificial dissipation was not needed.

2. Governing equations

Fig. 1 shows the schematic view of the cylinder's geometry and its thermal boundary conditions. According to this figure, the flow has two-dimensional characteristics. Therefore, the cylinder is assumed to have expanded adequately on the z axis. According to this figure, the cylinder cross section has a circle shape when $A = H/W = 1$. For other values of the aspect ratio, the cylinder cross section's shape will be elliptic. All cylinder walls are assumed to be nonslipping. Therefore, under these assumptions, the nondimensionless variables at the cylinder walls are obtained as $U = V = 0$ (for all walls), $\theta = 0$ (on the left wall), and $\theta = 1$ (on the right wall).

$$\frac{1}{\beta}\frac{\partial P}{\partial \zeta} + \frac{\partial U}{\partial X} + \frac{\partial V}{\partial Y} = 0 \qquad (1)$$

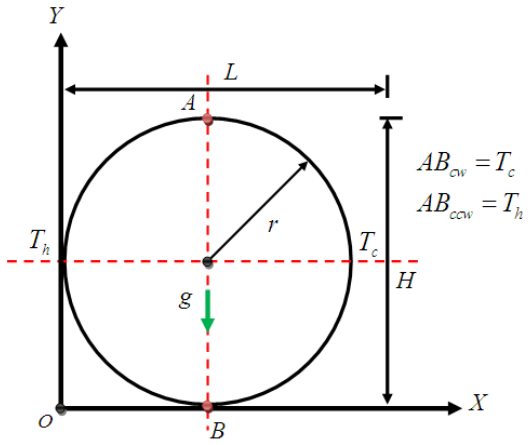

Fig. 1 Schematic view of the cylindrical cavity.

$$\frac{\partial U}{\partial \zeta}+\frac{\partial (UU)}{\partial X}+\frac{\partial (UV)}{\partial Y}=-\frac{\partial P}{\partial X}+\frac{\partial}{\partial X}\left(\Pr\frac{\partial U}{\partial X}\right)+\frac{\partial}{\partial Y}\left(\Pr\frac{\partial U}{\partial Y}\right), \quad (2)$$

$$\frac{\partial V}{\partial \zeta}+\frac{\partial (UV)}{\partial X}+\frac{\partial (VV)}{\partial Y}=-\frac{\partial P}{\partial Y}+\frac{\partial}{\partial X}\left(\Pr\frac{\partial V}{\partial X}\right)+\frac{\partial}{\partial Y}\left(\Pr\frac{\partial V}{\partial Y}\right)+\Pr Ra\theta, \quad (3)$$

$$\frac{\partial \theta}{\partial \zeta}+\frac{\partial (U\theta)}{\partial X}+\frac{\partial (V\theta)}{\partial Y}=\frac{\partial}{\partial X}\left(\frac{\partial \theta}{\partial X}\right)+\frac{\partial}{\partial Y}\left(\frac{\partial \theta}{\partial Y}\right), \quad (4)$$

The two-dimensional incompressible viscous flow governing equations in nondimensional form and with artificial compressibility can be written as

where $(U,V)=uL/\alpha,\ vL/\alpha$ are dimensionless Cartesian velocity components, $(X,Y)=x/L,\ y/L$ are dimensionless Cartesian axes, $P=pL^2/(\rho\alpha^2)$ is the dimensionless static pressure, $\theta=(T-T_c)/(T_h-T_C)$ is the dimensionless temperature, $A=H/L$ is the aspect cavity ratio, $\zeta=t\alpha/L^2$ is dimensionless time, *Pr* is the Prandtl number, *Ra* is the Raleigh number, and β is the artificial compressibility that is given as follows:

$$\frac{\partial \rho}{\partial t}=\frac{1}{\beta}\frac{\partial p}{\partial t}, \quad (5)$$

3. Formulation of heat-transfer characteristics

The volumetric entropy generation in the flow due to the heat transfer and fluid friction can be written as

$$\dot{S}_l=\dot{S}_{l.h}+\dot{S}_{l.f}, \quad (6)$$

The heat-transfer contribution of the volumetric entropy generation of the two-dimensional flow system is

$$\dot{S}_{l,h}=\frac{k}{T_0^2}\left[\left(\frac{\partial T}{\partial x}\right)^2+\left(\frac{\partial T}{\partial y}\right)^2\right], \quad (7)$$

The fluid-friction contribution of the volumetric entropy generation of the two-dimensional flow system is

$$\dot{S}_{l,f}=\frac{\mu}{T_0}\left[2\left(\frac{\partial u}{\partial x}\right)^2+2\left(\frac{\partial v}{\partial y}\right)^2+\left(\frac{\partial u}{\partial y}+\frac{\partial v}{\partial x}\right)^2\right], \quad (8)$$

The dimensionless quantity of these equations can be written as follows:

$$\dot{S}_{l.a}=\dot{S}_{l.a.h}+\dot{S}_{l.a.f}, \quad (9)$$

$$\dot{S}_{l.a.h}=\left[\left(\frac{\partial \theta}{\partial X}\right)^2+\left(\frac{\partial \theta}{\partial Y}\right)^2\right], \quad (10)$$

$$\dot{S}_{l.a.f}=\varphi\left[2\left(\frac{\partial U}{\partial X}\right)^2+2\left(\frac{\partial V}{\partial X}\right)^2+\left(\frac{\partial U}{\partial Y}+\frac{\partial V}{\partial X}\right)^2\right], \quad (11)$$

where φ is the ratio between the viscous and thermal irreversibilities in the following equation:

$$\varphi=\frac{\mu T_0}{k}\left[\frac{\alpha}{L(T_h-T_c)}\right], \quad (12)$$

where $T_0=(T_h+T_c)/2$ is the bulk temperature. The dimensionless total entropy generation is the integral over the system volume of the dimensionless local entropy generation:

$$\dot{S}_{T.a}=\int \dot{S}_{l.a}dv, \quad (13)$$

The Bejan nondimensional number (*Be*) is defined as follows:

$$Be=\frac{\dot{S}_{l.a.h}}{\dot{S}_{l.a}}, \quad (14)$$

When $Be\geq 1/2$, the irreversibility due to the heat transfer dominates. For $Be\leq 1/2$, the irreversibility

due to the viscous effect dominates. For $Be = 1/2$, heat-transfer and fluid-friction entropy generation are equal.

4. Nusselt number

The heat-transfer coefficient in terms of the local Nusselt number (Nu) is defined as

$$Nu = -\frac{\partial \theta}{\partial n}, \tag{15}$$

where *n* denotes the normal direction to a plan. The local Nusselt number at the heat wall-plane (Nu_x, Nu_y) is defined as

$$Nu_x = -\left(\frac{\partial \theta}{\partial x}\right)_L, \tag{16}$$

$$Nu_y = -\left(\frac{\partial \theta}{\partial x}\right)_H, \tag{17}$$

Therefore, the average Nusselt number is calculated as follows:

$$\overline{Nu} = \frac{1}{L+H}\left[\int_0^L Nu_x dx + \int_0^H Nu_y dy\right], \tag{18}$$

5. Grid features

Here, grids are generated by using coding program as an easy method which is used in this investigation. In order to describe this method, first consider a circle with Cartesian *xy* coordinates, as shown in Fig. 2. In the customary way, this circle could be approximated by quadrilateral ABCD. In this case, four cells in the form of triangles OAB, OBC, OCD, and ODA result from the grid-generation procedure. In the new current method, the circle is approximated by square 1234. In this case, four cells in the form of squares OA2B, OB3C, OC4D, and OD1A result from the grid-generation procedure.

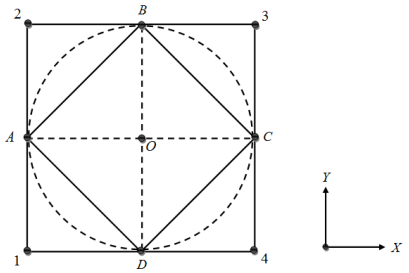

Fig. 2 Depiction of the current grid characteristics.

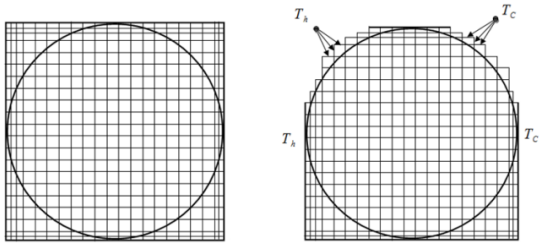

Fig. 3 Algebraic rectangular grids for a circular cavity.

Fig. 3 shows the grid-generation processes schematically for a circle cavity (i.e., A = 1) according to the following steps:

(1) As shown in Fig. 3a, the structured grid is generated algebraically for the square cavity. Clustering has been used near the square cavity walls.

(2) As shown in Fig. 3b, the cells in the vicinity of the curvilinear boundaries are selected completely as the computational domain (i.e., where pieces of them lay out of the physical domain). Then, the remaining cells between the curvilinear corner and the square cavity walls are withdrawn. Finally, all cells are established in the form of a rectangle.

(3) Now, the required boundary conditions can be imposed onto the extra cells' boundaries (see Fig. 3b).

6. Finite-volume scheme for space discretization

By integrating from conservation Eqs. (1)–(4) over a control volume Ω, which is bounded by surface $\partial\Omega$, and applying the Gauss divergence theorem, the following is derived:

$$\iint_\Omega \frac{1}{\beta}\frac{\partial P}{\partial \zeta} dS = -\oint_{\partial\Omega} (U dY - V dX), \tag{19}$$

$$\iint_\Omega \frac{\partial U}{\partial \zeta} dS = -\oint_{\partial\Omega} P dY - \int_{\partial\Omega} \left(U^2 dY - UV dX\right) + \Pr \int_{\partial\Omega} \left(\frac{\partial U}{\partial X} dY - \frac{\partial U}{\partial Y} dX\right), \tag{20}$$

$$\iint_\Omega \frac{\partial V}{\partial \zeta} dS = \oint_{\partial\Omega} P dX - \int_{\partial\Omega} \left(UV dY - V^2 dX\right) + \Pr \int_{\partial\Omega} \left(\frac{\partial V}{\partial X} dY - \frac{\partial V}{\partial Y} dX\right) + \Pr Ra\theta \iint_{\partial\Omega} dS, \tag{21}$$

$$\iint_\Omega \frac{\partial \theta}{\partial \zeta} dS = \int_{\partial\Omega} \left(\frac{\partial \theta}{\partial X} dY - \frac{\partial \theta}{\partial Y} dX\right) - \int_{\partial\Omega} (U\theta dY - V\theta dX), \tag{22}$$

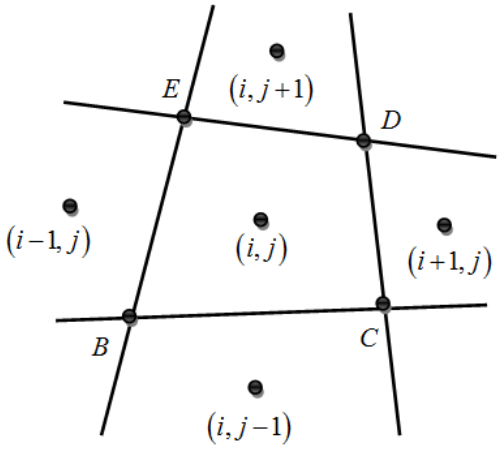

Fig. 4 Cell view in the finite-volume method.

Therefore, these equations can be arranged in the suitable vector form as follows:

$$\frac{\partial}{\partial\zeta}\iint_{\Omega} Q dS = -\oint_{\partial\Omega}\left(F dY - G dX\right) + \oint_{\partial\Omega}\left(R dY - W dx\right) + \iint_{\Omega} Z dS, \tag{23}$$

where

$$Q=\begin{pmatrix} P \\ U \\ V \\ \theta \end{pmatrix},\ F=\begin{pmatrix} \beta U \\ U^2+P \\ UV \\ U\theta \end{pmatrix},\ G=\begin{pmatrix} \beta V \\ UV \\ V^2+P \\ V\theta \end{pmatrix},$$
$$\mathrm{R}=\begin{pmatrix} 0 \\ \mathrm{Pr}\dfrac{\partial U}{\partial X} \\ \mathrm{Pr}\dfrac{\partial V}{\partial X} \\ \dfrac{\partial\theta}{\partial X} \end{pmatrix},\ \mathrm{W}=\begin{pmatrix} 0 \\ \mathrm{Pr}\dfrac{\partial U}{\partial Y} \\ \mathrm{Pr}\dfrac{\partial V}{\partial Y} \\ \dfrac{\partial\theta}{\partial Y} \end{pmatrix},\ \mathrm{Z}=\begin{pmatrix} 0 \\ 0 \\ \mathrm{PrRa}\theta \\ 0 \end{pmatrix}, \tag{24}$$

The computational domain is divided into rectangular cells (see Fig. 4), and a system of ordinary differential equations is obtained by applying Eq. (23) to each cell separately.

In order to find the convective terms in the boundaries of the cell (i,j), we choose the custom flux averaging scheme. In this scheme, each quantity, such as $(u\theta)_1$ (i.e., the value of $u\theta$ on the boundary denoted by number 1, as shown in Fig. 4), is evaluated as the average of the cells on either side of the face, that is $(u\theta)_1 = 1/2[(u\theta)_{i,j} + (u\theta)_{i,j-1}]$.

Flux averaging is applied here for the viscous and conduction terms. In this method, we need to know the first-order derivatives, such as $(\partial\theta/\partial y)_{i,j}$ and so on (at the cell centers). These functions are obtained from the Gauss divergence theorem. For example, we have $(\partial\theta/\partial y)_{i,j} = -1/S_{i,j}\oint_{\partial\Omega}\theta\, dx$. Therefore, these derivatives are saved for all cells as the functions that can be used in the next time step. Thus, each quantity, for example, $(\partial\theta/\partial y)_1$, is found, such as $(\partial\theta/\partial y)_1 = 1/2[(\partial\theta/\partial y)_{i,j} + (\partial\theta/\partial y)_{i,j-1}]$ and so on.

After discretizing Eq. (23) around the cell (i,j) and considering the cell-centered assumption for the variables, the following are the results:

$$S_{i,j}\frac{\partial Q_{i,j}}{\partial\zeta} = -\sum_{k=1}^{4}\left(F_{i,j}\Delta Y - G_{i,j}\Delta X\right)_k + \sum_{k=1}^{4}\left(R_{i,j}\Delta Y - W_{i,j}\Delta X\right)_k + S_{i,j}Z_{i,j}, \tag{25}$$

where $S_{i,j}$ is the area of the cell (i,j).

7. Numerical solution processes

An explicit classical fourth-order Runge–Kutta integration algorithm was applied to ordinary differential Eq. (25) to find the steady-state condition. To study the effect of the grid size on the solutions, a series of calculations was performed by varying the number of grid points in each direction. For $A=1$, it was found that, at $Ra=10^3$, the Bejan number changes less than 0.0867 percent as the grid point varies from 50×50 to 150×150. Therefore, 100×100 grid points are considered optimal for this study. For the case $A\neq1$, the grid points were adjusted according to the aspect-ratio (A) values. The convergence criterion was used for the mass conservation residue, established as 10^{-8}. In this study, the selected fluid flow is air (with Pr = 0.7).

8. Results and discussions

In order to show the validation of this study, the code was reproduced to solve a similar problem in [8] (i.e., $H=W=1$ and the square boundary cavity). Then, the mean Nusselt number values for different Ra numbers were compared between the present study and the literature, as seen in Table 1. It can be seen that the results obtained from the present model are as good as were expected.

The curves in Fig. 5 show the histories of the mass conservation residues (Res) for different values of the artificial compressibility parameters ( ) in the cases of different aspect ratios and different Rayleigh numbers. One can see that, in all situations, good convergence speed has been obtained. Also, for each selected value of , in the case of the constant aspect ratio, the residues are converged with the constant number. This means that the value of cannot change the exactness of the steady-state results. However, the convenience choice of can be useful for the solution procedure.

The streamline is shown in Fig. 6, which depicts three different aspect ratios ($A = 0.5, 1, 2$) in the cases of two Rayleigh numbers ($Ra = 10^3, 10^5$). In all figures, it can be observed that, with an increase in the Rayleigh number, the circulation of the fluid flow is affected by the thickness of the hydrodynamic boundary layer. This phenomenon is followed by an increase in the fluid acceleration due to the buoyant force action layers.

Isotherms have been plotted in Fig. 7. These figures have been sketched for three different aspect ratios ( ) in the cases of two Rayleigh numbers ( ). We know that the temperature gradient causes these phenomena. It can be seen that the variation of the aspect ratio affects the temperature distribution within the cylinder. For a small Rayleigh number (i.e.,), the isolines are approximately smooth and vertical. In a high Rayleigh number (i.e.,), the isolines are horizontal at the cavity center and vertically clustered near the isotherm's boundary walls. In the natural convection process, the biggest velocity gradients are found near the walls that have larger thermal gradients due to the action of the buoyant force.

Table. 1 Verifying for average Nusselt number.

	$Ra = 10^3$	$Ra = 10^4$	$Ra = 10^5$	$Ra = 10^6$
Ref. [8]	1.116	2.239	4.531	8.721
Present work	1.117	2.244	4.522	8.830
Deviation (%)	0.1	0.5	0.9	0.11

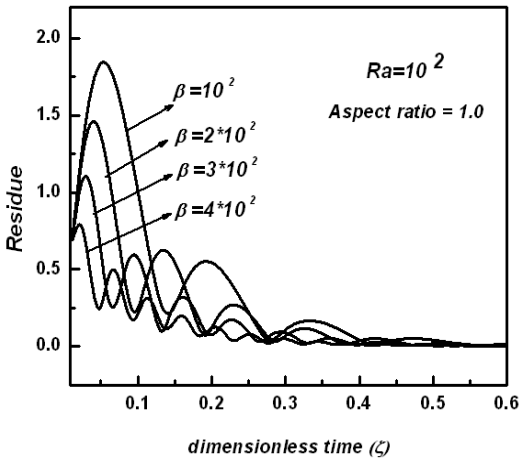

Fig. 5 Histories of the mass conservation residues.

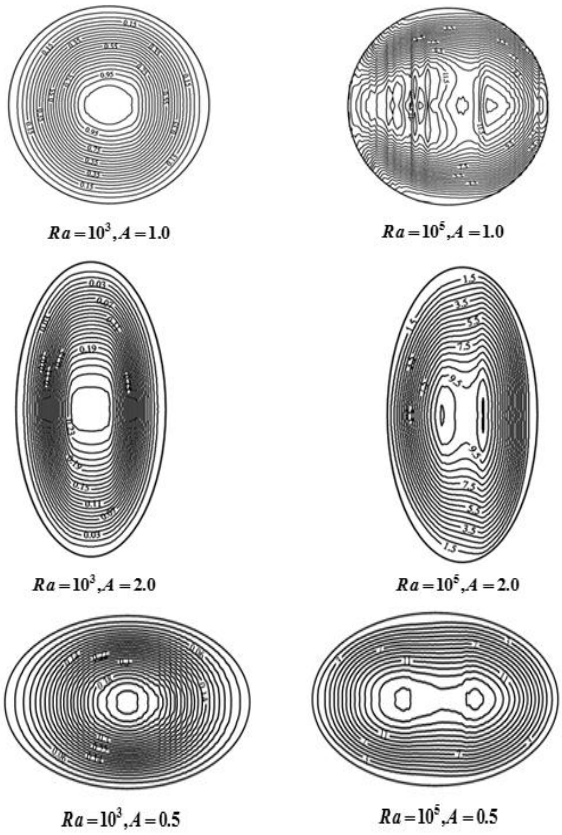

Fig. 6 The velocity field for $Ra = 10^3$ and $Ra = 10^5$ in different aspect ratios (A).

The effects of the irreversibility ratio and the Rayleigh number on the total entropy generation ( ) are shown in Fig. 9. These figures have been drawn for different aspect ratios ( ). According to these figures, a higher aspect ratio has a greater entropy generation. Also, it can be seen that, with a decrease in the irreversibility ratio, the total entropy generation decreases. In addition, according to these figures, for a higher Rayleigh number, the values of the total entropy generation limit the constant value.

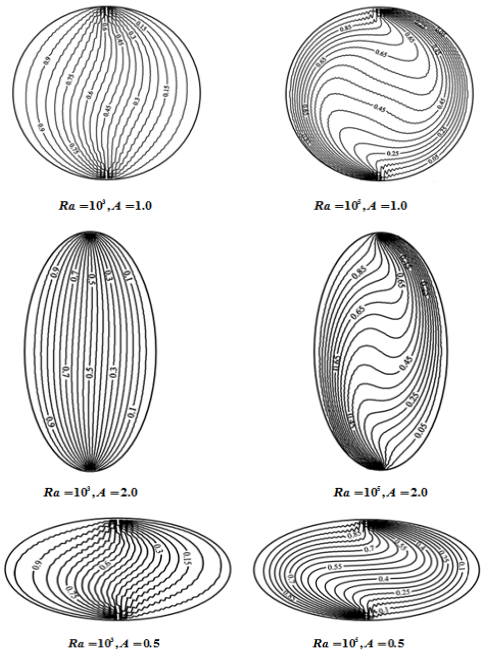

Fig. 7 Isotherms for $Ra = 10^3$ and $Ra = 10^5$ in different aspect ratios (A).

Fig. 8 shows isobars for different aspect ratios and Rayleigh numbers. The figure clearly illustrates how a stratified pressure field is formed. In the case of both a higher aspect ratio and Rayleigh number, the isobars are horizontal.

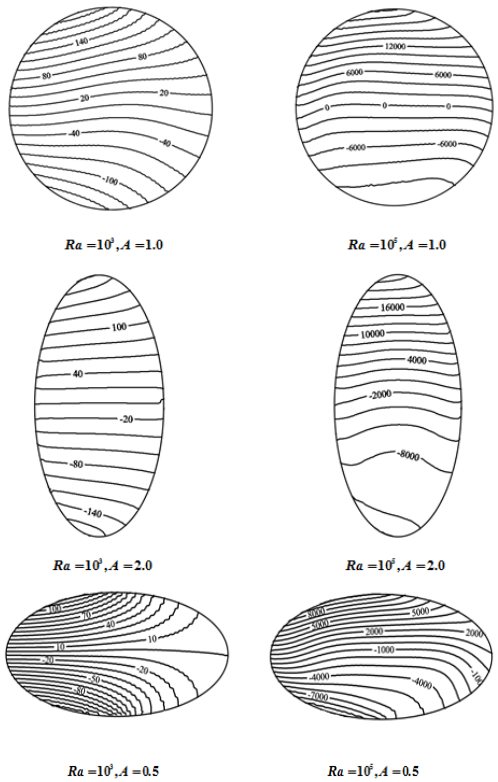

Fig. 8 Isobars for $Ra = 10^3$ and $Ra = 10^5$ in different aspect ratios (A).

The effects of the aspect ratio, irreversibility ratio, and the Rayleigh number on the Bejan nondimensional number (Be) are shown in Fig. 10. Different behaviors are shown for the variation of the Bejan nondimensional number when the irreversibility ratio changes. It can be seen that, with a decrease in the irreversibility ratio, the Bejan number increases. This phenomenon obviously can be seen with a high Rayleigh number. As mentioned previously, when , the irreversibility due to the heat transfer dominates. For , the irreversibility due to the viscous effect dominates. For , heat-transfer and fluid-friction entropy generation are equal.

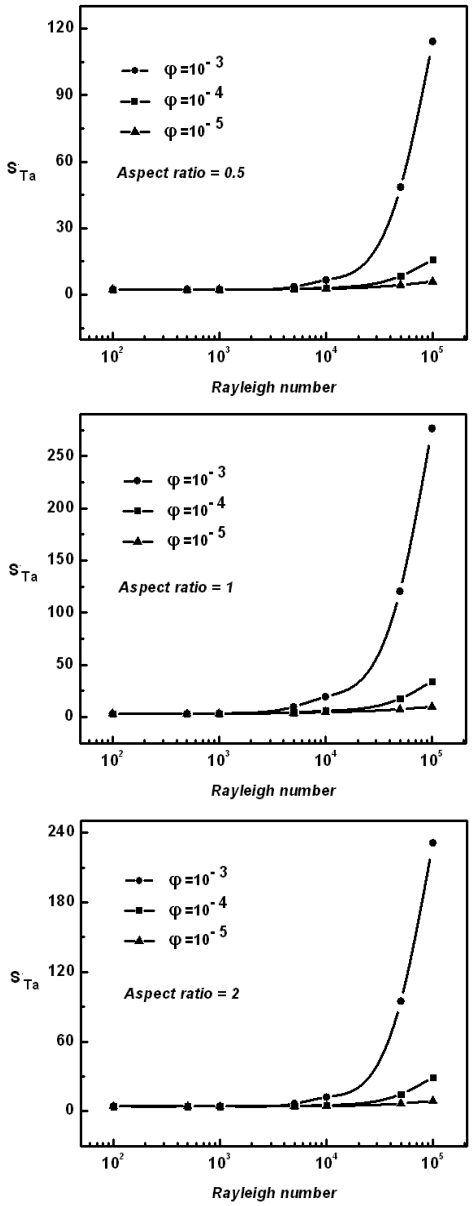

Fig. 9 The effects of the irreversibility ratio (φ), aspect ratio (A), and the Rayleigh number on the total entropy generation ($\dot{S}_{Ta}$).

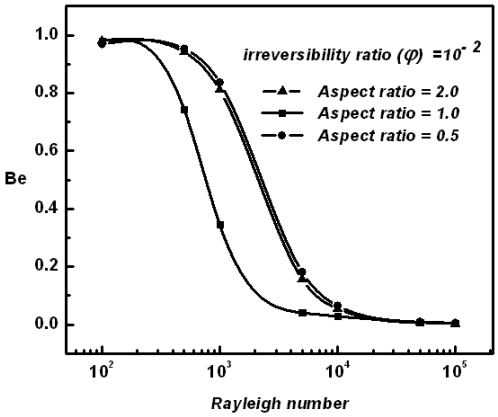

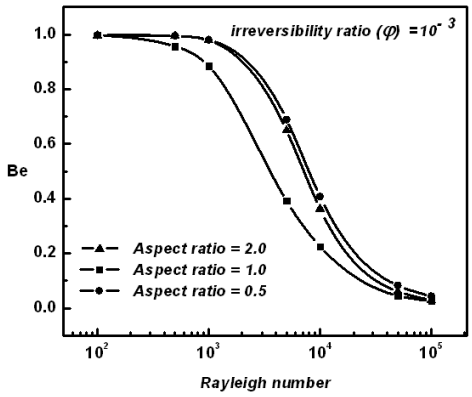

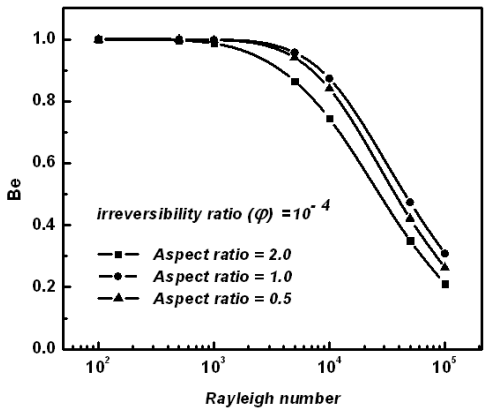

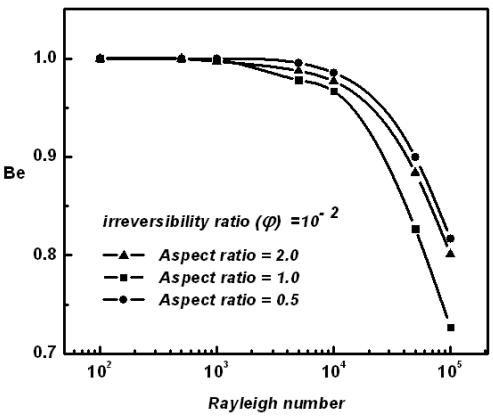

Fig. 10 The effects of the irreversibility ratio (φ), aspect ratio (A), and the Rayleigh number on the Bejan number (Be).

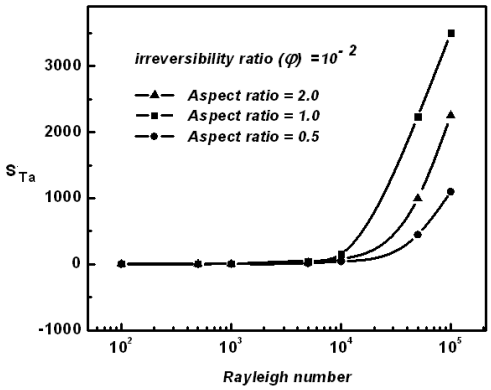

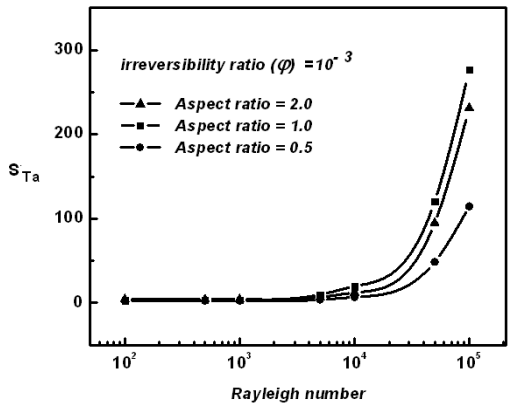

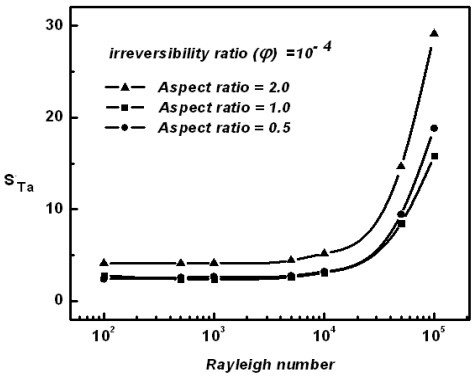

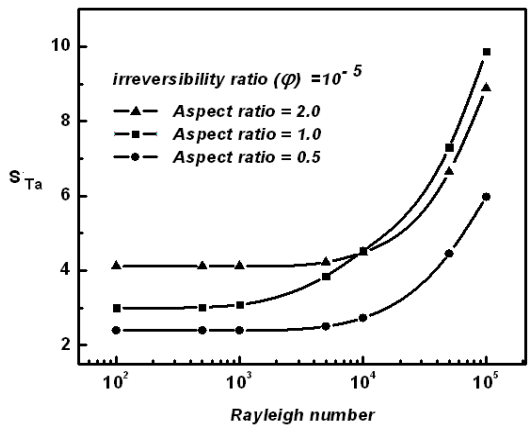

Fig. 11 The effects of the aspect ratio (A), irreversibility ratio (φ), and the Rayleigh number on the total entropy generation ($\dot{S}_{Ta}$).

The effects of the aspect ratio and the Rayleigh number on the total entropy generation ( ) are shown in Fig. 11. These figures have been drawn for different irreversibility ratios . According to these figures, a higher irreversibility ratio has a bigger entropy generation. Also, it can be seen that, with an increase in the aspect ratio, the total entropy generation increases. In addition, according to these figures, with a higher Rayleigh number, the values of the total entropy generation increase exponentially as a function, and with a lower Rayleigh number, the values of the total entropy generation limit the constant value.

The effects of the aspect ratio, irreversibility ratio, and the Rayleigh number on the nondimensional Nusselt number (Nu) are shown in Fig. 12. Different behaviors are shown for variations of the Nusselt number when the aspect ratio changes. Due to the low temperature gradient, the Nusselt number is not high when there is a low Rayleigh number. When the temperature gradient increases, the Rayleigh number also increases, and as a result, the Nusselt number enhances exponentially as a function. When the Rayleigh number gradually increases, the buoyancy force intensifies, and finally, the dominant force and the viscosity of the fluid will begin to move. Increasing the Rayleigh number in all cases will increase the amount of the buoyancy force, or the turbulence of the flow within the chamber.

Also, one can try to correlate functions for the Nusselt number through the curves shown in Fig. 12. For example, the following equation results under the related conditions:

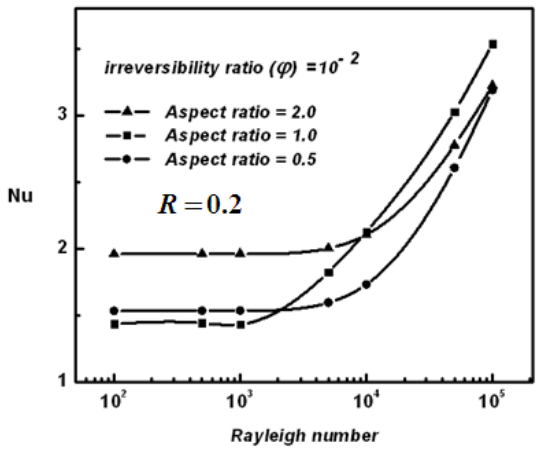

Fig. 12 The effects of the aspect ratio ( ) and the Rayleigh number on the Nusselt number.

$Nu = 0.79Ra^{0.103}$ for $10^2 < Ra < 10^5$, $\Pr = 0.7$, and $Aspect\ ratio = 0.5$;

$Nu = 0.62Ra^{0.14}$ for $10^2 < Ra < 10^5$, $\Pr = 0.7$, and $Aspect\ ratio = 1.0$; and

$Nu = 1.26Ra^{0.007}$ for $10^2 < Ra < 10^5$, $\Pr = 0.7$, and $Aspect\ ratio = 2.0$.

9. Conclusions

In this paper, an explicit finite-volume model was developed to study incompressible natural convection in cylindrical cavities. An artificial compressibility technique was applied to couple continuity with momentum equations. In order to find the steady-state solutions, an explicit classical fourth-order Runge–Kutta integration algorithm was applied to the ordinary differential, obtained from a cell-centered finite-volume discretization scheme (see Eq. (25)). In this work, the aspect ratio, the Rayleigh number, and the irreversibility distribution ratio were limited as $0.5 < A < 2$, $10^2 < Ra < 10^5$, and $10^{-2} < \varphi < 10^{-5}$, respectively. It was seen that, with a decrease in the irreversibility ratio, the total entropy generation decreases. Different behaviors are shown for variations of the Bejan nondimensional number when the irreversibility ratio changes. It was seen that, with a decrease in the irreversibility ratio, the Bejan number increases.

Nomenclature

A	aspect ratio, dimensionless
C_p	specific heat at constant pressure, J/kgK
Be	Bejan number, dimensionless
β	thermal expansion coefficient, $1/K$
g	gravitational acceleration, m/s^2
h	heat-transfer coefficient, W/m^2K
H	cavity height, m
k	thermal conductivity, W/mK
L	cavity length, m
Nu	Nusselt number, dimensionless
p	pressure, Pa
P	dimensionless pressure
Pr	Prandtl number, dimensionless
Ra	Rayleigh number, dimensionless

$\dot{S}$	entropy generation, W/m^3K
t	time, s
T	temperature, K
R	cavity corner radius, m
r	dimensionless radius
u,v	velocity components in x,y direction, m/s
U,V	dimensionless velocity, components in x,y direction
x,y	Cartesian coordinates, m
	dimensionless Cartesian coordinates X,Y

Greek Symbols

α	thermal diffusivity, m^2/s
γ	artificial compressibility
μ	dynamic viscosity, kg/ms
v	kinematics viscosity, m^2/s
ρ	density, kg/m^3
ζ	dimensionless time
θ	dimensionless temperature
φ	irreversibility ratio, dimensionless

Subscripts

a	dimensionless
c	cold
f	fluid viscous effect
h	hot
l	local
T	total

References

[1] M. Salari, A. Rezvani, A. Mohammadtabar, and M. Mohammadtabar, "Numerical Study of Entropy Generation for Natural Convection in Rectangular Cavity with Circular Corners," *Heat Transfer Engineering*, vol. 36, pp. 186-199, 8/ 2014.

[2] D. K. Edwards and I. Catton, "Prediction of heat transfer by natural convection in closed cylinders heated from below," *International Journal of Heat and Mass Transfer*, vol. 12, pp. 23-30, 1/ 1969.

[3] A. Horibe, R. Shimoyama, N. Haruki, and A. Sanada, "Experimental study of flow and heat transfer characteristics of natural convection in an enclosure with horizontal parallel heated plates," *International Journal of Heat and Mass Transfer*, vol. 55, pp. 7072-7078, 11/ 2012.

[4] B. M. Ziapour and R. Dehnavi, "A numerical study of the arc-roof and the one-sided roof enclosures based on the entropy generation minimization," *Computers & Mathematics with Applications*, vol. 64, pp. 1636-1648, 9/ 2012.

[5] B. M. Ziapour and R. Dehnavi, "Finite-volume method for solving the entropy generation due to air natural convection in -shaped enclosure with circular corners," *Mathematical and Computer Modelling*, vol. 54, pp. 1286-1299, 9/ 2011.

[6] R. Dehnavi and A. Rezvani, "Numerical investigation of natural convection heat transfer of nanofluids in a Γ shaped cavity," *Superlattices and Microstructures*, vol. 52, pp. 312-325, 8/ 2012.

[7] I. Rashidi, O. Mahian, G. Lorenzini, C. Biserni, and S. Wongwises, "Natural convection of Al2O3/water nanofluid in a square cavity: Effects of heterogeneous heating," *International Journal of Heat and Mass Transfer*, vol. 74, pp. 391-402, 7/ 2014.

[8] R. D. C. Oliveski, M. H. Macagnan, and J. B. Copetti, "Entropy generation and natural convection in rectangular cavities," *Applied Thermal Engineering*, vol. 29, pp. 1417-1425, 6/ 2009.

[9] I. Dagtekin, H. F. Oztop, and A. Bahloul, "Entropy generation for natural convection in Γ-shaped enclosures," *International Communications in Heat and Mass Transfer*, vol. 34, pp. 502-510, 4/ 2007.

[10] S. K. Pandit and A. Chattopadhyay, "Higher order compact computations of transient natural convection in a deep cavity with porous medium," *International Journal of Heat and Mass Transfer*, vol. 75, pp. 624-636, 8/ 2014.

[11] Y. Liu, C. Lei, and J. C. Patterson, "Natural convection in a differentially heated cavity with two horizontal adiabatic fins on the sidewalls," *International Journal of Heat and Mass Transfer*, vol. 72, pp. 23-36, 5/ 2014.

[12] É. Fontana, A. d. Silva, and V. C. Mariani, "Natural convection in a partially open square cavity with internal heat source: An analysis of the opening mass flow," *International Journal of Heat and Mass Transfer*, vol. 54, pp. 1369-1386, 3/ 2011.

[13] J. V. C. Vargas and A. Bejan, "Thermodynamic optimization of the match between two streams with phase change," *Energy*, vol. 25, pp. 15-33, 1/ 2000.

[14] J. J. Flores, G. Alvarez, and J. P. Xaman, "Thermal performance of a cubic cavity with a solar

control coating deposited to a vertical semitransparent wall," *Solar Energy*, vol. 82, pp. 588-601, 7/ 2008.

[15] L. Chen, Q. Xiao, Z. Xie, and F. Sun, "Constructal entransy dissipation rate minimization for tree-shaped assembly of fins," *International Journal of Heat and Mass Transfer*, vol. 67, pp. 506-513, 12/ 2013.

[16] S. Chen and M. Krafczyk, "Entropy generation in turbulent natural convection due to internal heat generation," *International Journal of Thermal Sciences*, vol. 48, pp. 1978-1987, 10/ 2009.

[17] A. Bradji, "A full analysis of a new second order finite volume approximation based on a low-order scheme using general admissible spatial meshes for the unsteady one dimensional heat equation," *Journal of Mathematical Analysis and Applications*, vol. 416, pp. 258-288, 1/ 2014.

[18] Z. Zhang, X. Zhang, and J. Yan, "Manifold method coupled velocity and pressure for Navier–Stokes equations and direct numerical solution of unsteady incompressible viscous flow," *Computers & Fluids*, vol. 39, pp. 1353-1365, 9/ 2010.

[19] R. K. Shukla, M. Tatineni, and X. Zhong, "Very high-order compact finite difference schemes on non-uniform grids for incompressible Navier–Stokes equations," *Journal of Computational Physics*, vol. 224, pp. 1064-1094, 10/ 2007.

[20] F. Bassi, A. Crivellini, D. A. Di Pietro, and S. Rebay, "An artificial compressibility flux for the discontinuous Galerkin solution of the incompressible Navier–Stokes equations," *Journal of Computational Physics*, vol. 218, pp. 794-815, 1/ 2006.

[21] V. Esfahanian and P. Akbarzadeh, "The Jameson's numerical method for solving the incompressible viscous and inviscid flows by means of artificial compressibility and preconditioning method," *Applied Mathematics and Computation*, vol. 206, pp. 651-661, 12/ 2008.

[22] A. J. Chorin, "A numerical method for solving incompressible viscous flow problems," *Journal of Computational Physics*, vol. 2, pp. 12-26, 8/ 1967.

[23] L. Ge and F. Sotiropoulos, "A numerical method for solving the 3D unsteady incompressible Navier–Stokes equations in curvilinear domains with complex immersed boundaries," *Journal of Computational Physics*, vol. 225, pp. 1782-1809, 10/ 2007.

[24] K. T. Yoon, S. Y. Moon, S. A. Garcia, G. W. Heard, and T. J. Chung, "Flowfield-dependent mixed explicit-implicit (FDMEI) methods for high and low speed and compressible and incompressible flows," *Computer Methods in Applied Mechanics and Engineering*, vol. 151, pp. 75-104, 1/ 1998.

[25] S. Yoon and D. Kwak, "Implicit methods for the Navier-Stokes equations," *Computing Systems in Engineering*, vol. 1, pp. 535-547, 2/ 1990.

[26] F. Xiao, R. Akoh, and S. Ii, "Unified formulation for compressible and incompressible flows by using multi-integrated moments II: Multi-dimensional version for compressible and incompressible flows," *Journal of Computational Physics*, vol. 213, pp. 31-56, 3/ 2006.

[27] S. Kaushik and S. G. Rubin, "Incompressible navier-stokes solutions with a new primitive variable solver," *Computers & Fluids*, vol. 24, pp. 27-40, 1/ 1995.

[28] H. S. Tang and F. Sotiropoulos, "Fractional step artificial compressibility schemes for the unsteady incompressible Navier–Stokes equations," *Computers & Fluids*, vol. 36, pp. 974-986, 6/ 2007.

[29] A. Shah, L. Yuan, and S. Islam, "Numerical solution of unsteady Navier–Stokes equations on curvilinear meshes," *Computers & Mathematics with Applications*, vol. 63, pp. 1548-1556, 6/ 2012.

[30] A. Shah, L. Yuan, and A. Khan, "Upwind compact finite difference scheme for time-accurate solution of the incompressible Navier–Stokes equations," *Applied Mathematics and Computation*, vol. 215, pp. 3201-3213, 1/ 2010.

[31] C. Kiris and D. Kwak, "Numerical solution of incompressible Navier–Stokes equations using a fractional-step approach," *Computers & Fluids*, vol. 30, pp. 829-851, 9/ 2001.

[32] M. Breuer and D. Hänel, "A dual time-stepping method for 3-d, viscous, incompressible vortex flows," *Computers & Fluids*, vol. 22, pp. 467-484, 7/ 1993.

[33] J.-g. Lin, Z.-h. Xie, and J.-t. Zhou, "Application of a three-point explicit compact difference scheme to the incompressible navier-stokes equations," *Journal of Hydrodynamics, Ser. B*, vol. 18, pp. 151-156, 7/ 2006.